Supporting information

High-capacity aqueous imidazolium-ion battery enabled by MMZ-H^+/H^+ co-intercalation in a near neutral electrolyte

Haiping Yu,[a,b] Rui Li,[a,b] Zhihui Wang,[c] Bei Wang,[a,b] Mengxiao Li,[c] Guoqing Zhao,[c] Xinyu Wang,[a,b] Xiaorong Yan,[c] Yuxin Hao,[a,b] Huige Ma,[a,b] Jingru Liu,[a,b] Mingjun Hu,[,c] Jun Yang[*,a,d]*

a Beijing Institute of Nanoenergy & Nanosystems, Chinese Academy of Sciences, Beijing, 101400, China.

b School of Nanoscience and Engineering, University of Chinese Academy of Sciences, Beijing,101408, China.

c School of Materials Science and Engineering, Beihang University, Beijing 100191, China.

d Shenzhen Institute for Advanced Study, University of Electronic Science and Technology of China, Shenzhen, 518000, China.

[*]Corresponding author, E-mail: mingjunhu@buaa.edu.cn, yangjun@binn.cas.cn.

1. Materials and Methods

1.1 Materials

Triquinoyl hydrate (99%) was purchased from Bidepharm. 3,4-Diaminobenzonitrile (97%), 1,3-Dimethylimidazolium chloride (98%) and 1-methylimidazole (99%) were obtained from Macklin. Manganese sulphate (98%) and 1-methyl-1,2,4-triazole (98%) were purchased by Aladdin. Sulfuric acid (98%) was purchased from TCI Chemicals. Glass fiber separator (GF/A, 4.7 cm) was obtained from Whatman. Ketjen black, activated carbon and polyvinylidene difluoride (PVDF) were purchased from Canrd Technology Co. Ltd. All the solvents were purchased from Aladdin and used as received without further purification.

1.2 General methods

1H nuclear magnetic resonance (NMR) spectra were tested on a Bruker AVANCE IIIHD500 (Bruker, Germany). Powder X-ray diffraction (PXRD) were recorded on a Xpert3 Powder (PANalytical, Holland) with Cu Kα radiation (λ = 1.5418Å). High resolution mass spectra (HRMS) were recorded with a LCMS-IT-TOF (Shimadzu, Japan). Fourier transform infrared (FT-IR) spectra were performed on a Bruker VERTEX80v (Bruker, Germany). Raman spectra were collected at Horiba LabRAM HR Evolution (HORIBA Scientific, Japan) with a laser wavelength of 532 nm. The scanning electron microscopy (SEM) characterizations were performed on a ZEISS Sigma 300 (ZEISS, Germany). Transmission electron microscope (TEM) measurements were conducted using a JEM-F200 (JEOL, Japan). X-ray photoelectron spectroscopy (XPS) measurements were performed on a Fisher Scientific ESCALAB Xi (Thermo, USA), The viscosities were performed on a Rheometer MCR 302 (Anton Paar, Austria).

1.3 Molecular dynamics (MD) simulations

Quantum chemistry calculations were first performed to optimize molecular geometries of MMZ solvent molecule using the Gaussian 16 package[1] at B3LYP/6-311+G(d) level of theory. The atomic partial charges on these solvent molecules were computed by fitting to the molecular electrostatic potential at atomic centers with the Møller-Plesset second-order perturbation method and the correlation-consistent

polarized valence cc-pVTZ(-f) basis set. The atomistic force field parameters for all ions and molecules are described by the AMBER format and are taken from previous work.[2] The cross-interaction parameters between different atom types are obtained from the Lorentz-Berthelot combination rule.

A modelling system consisting of 40 H_2SO_4 ion pairs, 200 MMZ, and 4320 water molecules was constructed. The SPC/E water model was adopted in the current work. Atomistic simulations of this modelling system were performed using GROMACS package with cubic periodic boundary conditions.[3] The equations for the motion of all atoms were integrated using a classic Verlet leapfrog integration algorithm with a time step of 1.0 fs. A cutoff radius of 1.5 nm was set for short-range van der Waals interactions and real-space electrostatic interactions. The particle-mesh Ewald (PME) summation method with an interpolation order of 5 and a Fourier grid spacing of 0.12 nm was employed to handle long range electrostatic interactions in reciprocal space. All simulation systems were first energetically minimized using a steepest descent algorithm, and thereafter annealed gradually from 600 K to 300 K within 5 ns. All annealed simulation systems were equilibrated in an isothermal-isobaric (NPT) ensemble for 10 ns of physical time maintained using a Nosé-Hoover thermostat and a Parrinello-Rahman barostat with time coupling constants of 0.5 and 0.3 ps, respectively, to control the temperature at 300 K, and the pressure at 1 atm. Atomistic simulations were further performed in a canonical ensemble (NVT) for 40 ns, and simulation trajectories were recorded at an interval of 100 fs for further structural and dynamical analysis, and to extract representative solvation structures.

1.4 Density functional theory (DFT) calculations

Density functional theory (DFT) calculations were carried out using Vienna Ab-initio Simulation Package (VASP).[4] The whole system contains a complete graphical interface for setting up, running and analyzing VASP calculations. The projected augmented wave (PAW) potential was employed to describe the core electrons, and the calculations were performed within the framework of the generalized gradient approximation (GGA), specifically using the Perdew-Burke-Ernzerh (PBE) functional to calculate the exchange-correlation energy. [5] The plane wave basis set was extended

with a cut-off energy of 450 eV. A 1×1×1 Monkhorst Pack k-point grid was utilized for structure optimizations and electronic structure calculations. The conjugate gradient method was employed to fully optimize the positions of the system until all forces on each atom were reduced to less than 0.02 eV/Å. The energy convergence of the whole self-consistent process was determined based on 10^{-5} eV. The gaussian smearing broadening was set to 0.05 eV. [6] The Electrostatic potential (ESP) and molecular structure were visualized using the VESTA.[7] The structure of the MMZ, MMZ-H^+ and diagram of two MMZ-H^+ insertions was optimized with gaussian 16.[1] Geometric optimizations were performed at B3LYP/6-31G(d,p) theoretical level[8] with All with Grimme's dispersion correction of D3 version (Becke-Johnson damping).[9] The size of the structure was calculated with Multiwfn.[10]

Table S1. The comparison between H_3O^+, Li^+, Na^+, K^+, NH_4^+, and Zn^{2+}ions.[11]

Characteristics	H_3O^+	Li^+	Na^+	K^+	NH_4^+	Zn^{2+}
Cation radius	1 Å	0.76 Å	1.02 Å	1.38 Å	1.48 Å	0.74 Å
Hydrated radius	N/A	3.82 Å	3.58 Å	3.31 Å	3.31 Å	4.3 Å

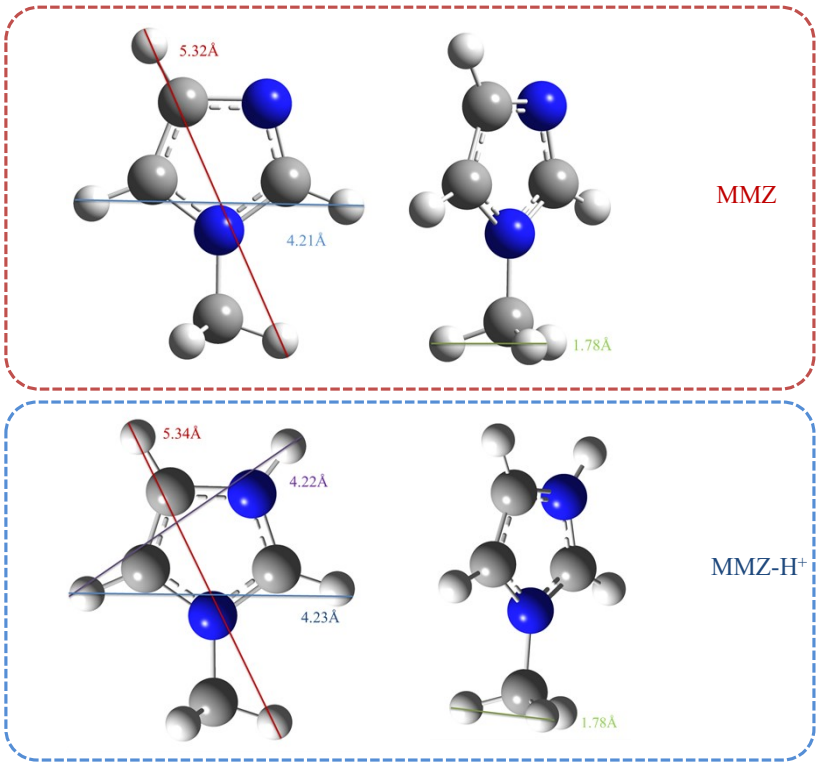

Figure S1. The ionic size of MMZ and MMZ-H^+.

1.5 Calculation details

The theoretical specific capacity of HATN-3CN can be calculated according to the equation as follow.

$$Q = \frac{nF}{3.6\,M} \qquad (1)$$

Where n is theoretical electron-transfer numbers of HATN-3CN, F is the Faraday constant, and M is the equivalent molecular weight of HATN-3CN (459.42 g mol^{-1}). Therefore, using Equation 1, the theoretical capacity of HATN-3CN is 350 mAh g^{-1}.

The ionic conductivity a series of electrolytes is calculated following the equations.

$$\sigma = \frac{L}{RS} \qquad (2)$$

Where σ refers to the ionic conductivity, L presents the thicknesses of the electrolyte, S is the area of the electrodes, R obtained from the Nyquist plot is the internal resistance of the electrolyte. Calculated values are summarised in Table S3.

Table S3. The ionic conductivity of a series of electrolytes at 25 °C.

Solution	Conductivity (mS cm^{-1})	Solution	Conductivity (mS cm^{-1})
0.5M H_2SO_4	219.6	62.5M-10S	106.8
12.5M-10S	193.2	125M-10S	40.6
25M-10S	202.8	250M-10S	37.8
50M-10S	254.4	MMZ in H_2O	4.3

1.6 Preparations of electrode materials

The HATN-3CN electrodes were prepared by mixing organic molecule with carbon black (Ketjen Black) and binder (PVDF) in a mass ratio of 60:30:10 in N-Methylpyrrolidone (NMP) solvent, and coating the slurry onto 12 mm diameter hydrophilic carbon paper and drying at 65 °C under vacuum. The small organic molecule mass load was around 1.5 mg cm^{-2}. The activated carbon (AC) membrane was prepared using the same way with a mass ratio of 80:10:10. When preparing the HATN-3CN electrodes for in situ and ex situ testing, the organic molecule, the Ketjen Black

and PVDF were blended in a mass ratio of 80:10:10 in NMP solvent. After coating the slurry onto 12 mm diameter hydrophilic carbon paper and drying at 65 ^{o}C under vacuum. After charging and discharging to the corresponding potential, the HATN-3CN electrodes were rinsed with water and ethanol repeatedly, followed by vacuum drying for ex-situ characterization. It should be noted that ex situ ^{1}H-NMR spectra were tested by dissolving the HATN-3CN electrodes in methyl sulfoxide-d6 (DMSO-d_6) reagent.

1.7 Electrochemical measurements

The half cells were assembled using Swagelok at three-electrode system using a HATN-3CN work electrode, activated carbon counter electrode and KCl-saturated Ag/AgCl ref. electrode, respectively. The full cells were tested at coin cells using HATN-3CN anode and MnO_2 cathode with the voltage range of 0-1.2 V. The pouch cell was designed and fabricated with HATN-3CN, MnO_2, glass microfiber and 0.5 M $MnSO_4$+50M-10S as anode, cathode, separator and electrolyte. Carbon cloth was working as current collector (3 x 3 cm) and tab at the same time. The loading mass of HATN-3CN is 16.2 mg. The linear sweep voltammetry (LSV), cyclic voltammetry (CV) and electrochemical impedance spectroscopy (EIS) measurements were performed on a CHI760e workstation. The EIS was tested with an AC amplitude of 5mV over a frequency ranging from 100 kHz to 0.1 Hz. The galvanostatic charge-discharge (GCD) tests were conducted on LAND-CT2001A battery testing instrument. The Galvanostatic Intermittent Titration Technique (GITT) measurements were carried out with a pulse of 2 min and a rest interval 5 min in a current density of 0.1 A g^{-1}.

2. Synthetic Procedures

2.1 Synthesis of Diquinoxalino[2,3-a:2',3',-c]phenazine-2,8,14-tricarbonitrile (HATN-3CN)

The HATN-3CN was synthesized by reference to the previously reported work.[12] ^{1}H NMR (400 MHz, DMSO-d_6): δ 9.21, 9.18, 8.77, 8.71, 8.69, 8.73, 8.42, 8.41. HR-

MS: m/z calculated for C27H9N9: 460.1; $[M + H]^+$ found: 460.10.

2.2 Preparation of 0.5 M H_2SO_4-MMZ electrolytes

Aqueous electrolytes were obtained by mixing MMZ solution in 0.5 M H_2SO_4 with stirring at room temperature. Electrolytes with different MMZ contents were shown in the table S2.

Table S2. The composition of a series of 0.5 M H_2SO_4-MMZ electrolytes.

name	MMZ mL	0.5M H_2SO_4 mL	pH	mole ratio (MMZ: H_2SO_4)
0.5M H_2SO_4	0	2	0.19	0:100
12.5M-10S	0.1	2	0.24	12.5:10
25M-10S	0.2	2	2.13	25:10
37.5M-10S	0.3	2	6.94	37.5:10
50M-10S	0.4	2	7.46	50:10
62.5M-10S	0.5	2	7.79	62.5:10
125M-10S	1	2	7.87	125:10
250M-10S	2	2	8.13	250:10
MMZ in H_2O	0.4	2 (H_2O)	10.81	50:0

Table S4. The viscosity of a series of electrolytes at 25ºC.

Solution	MMZ in H_2O	12.5M-10S	25M-10S	37.5M-10S	50M-10S	62.5M-10S	125M-10S	250M-10S
Viscosity/mPa*s	1.288	1.916	2.08	2.172	2.491	2.784	3.143	3.964

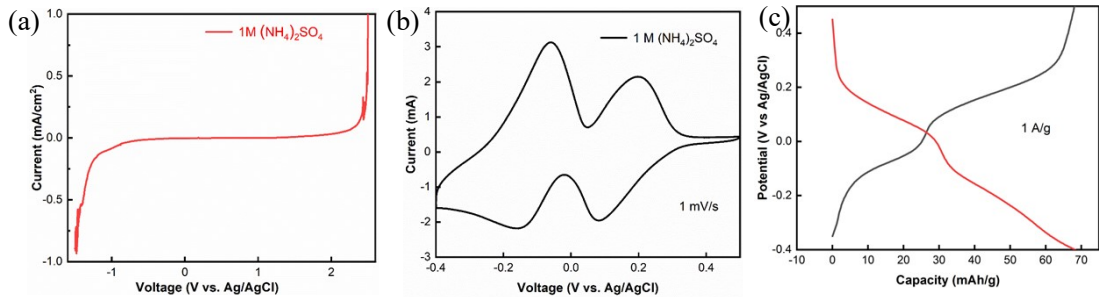

Figure S2. (a) The LSV curve and (b) CV curves (c) charge-discharge curve of HATN-3CN electrode in 1 M $(NH_4)_2SO_4$.

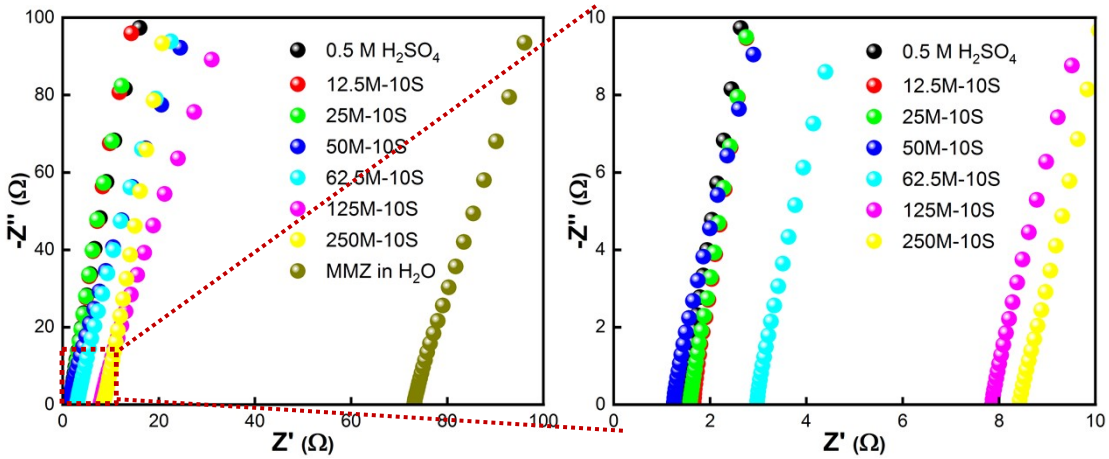

Figure S3. Nyquist plots of a series of electrolytes to obtain the ion conductivities.

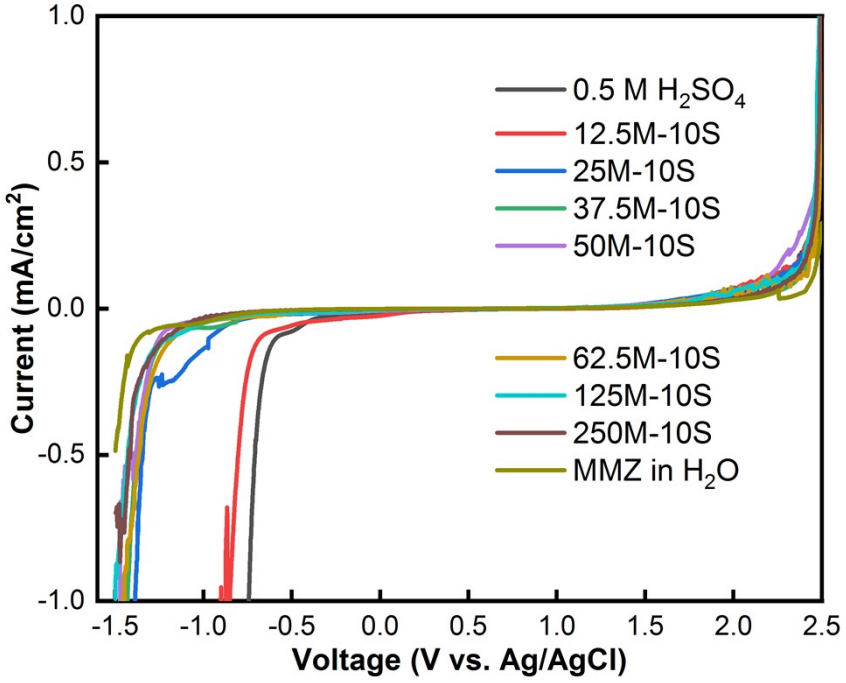

Figure S4. LSV curves of a series of electrolytes.

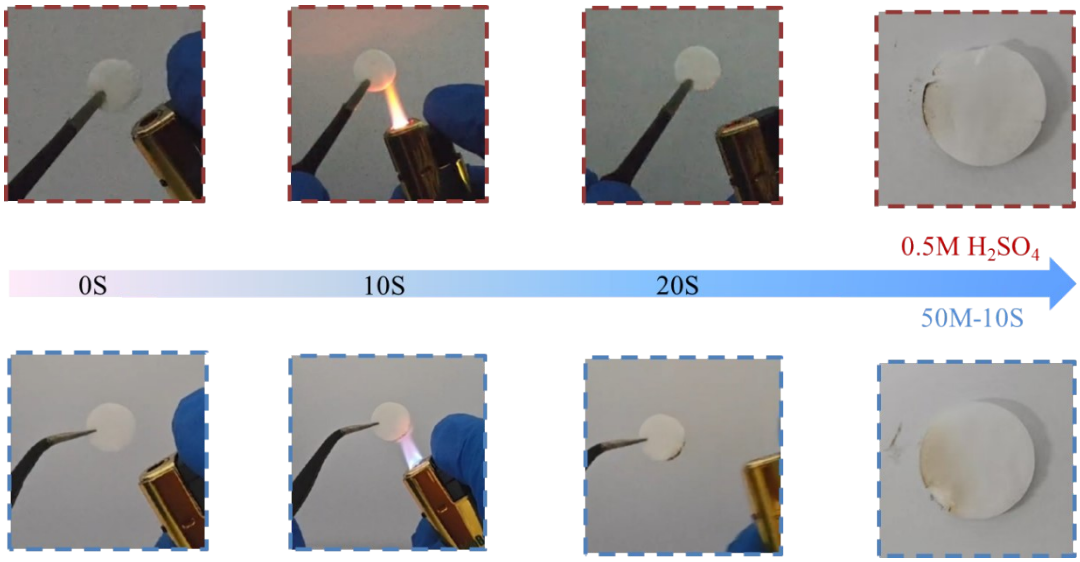

Figure S5. Combustion process of 0.5 M H_2SO_4 and 50M-10S electrolytes in 0-20 seconds.

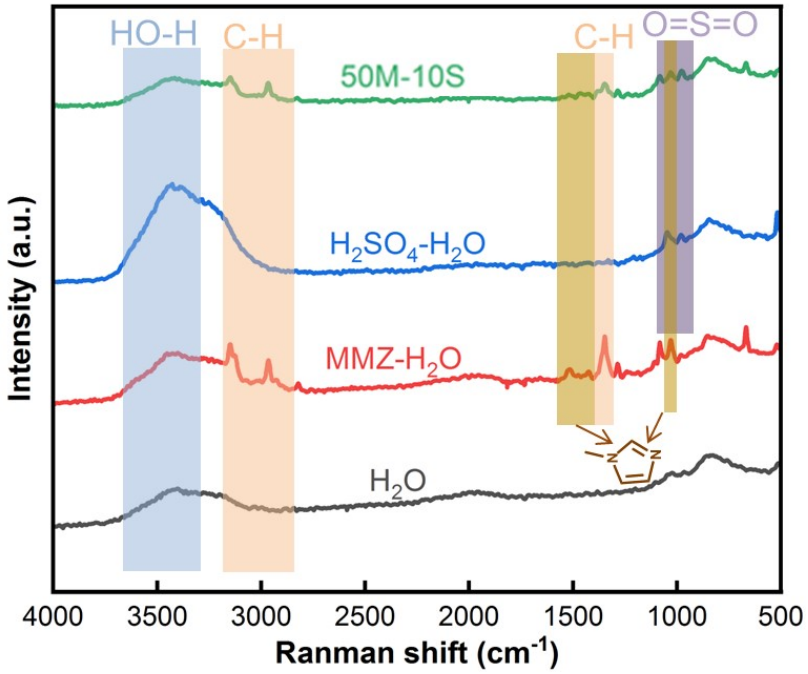

Figure S6. Raman spectra of contents in 50M-10S electrolyte.

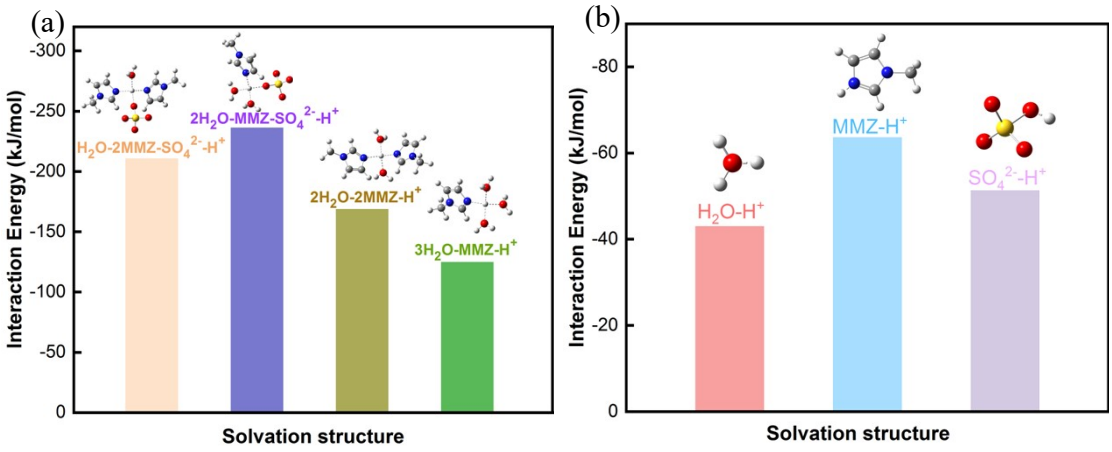

Figure S7. The binding energy of (a) a series of contents and (a) several configurations of electrolytes.

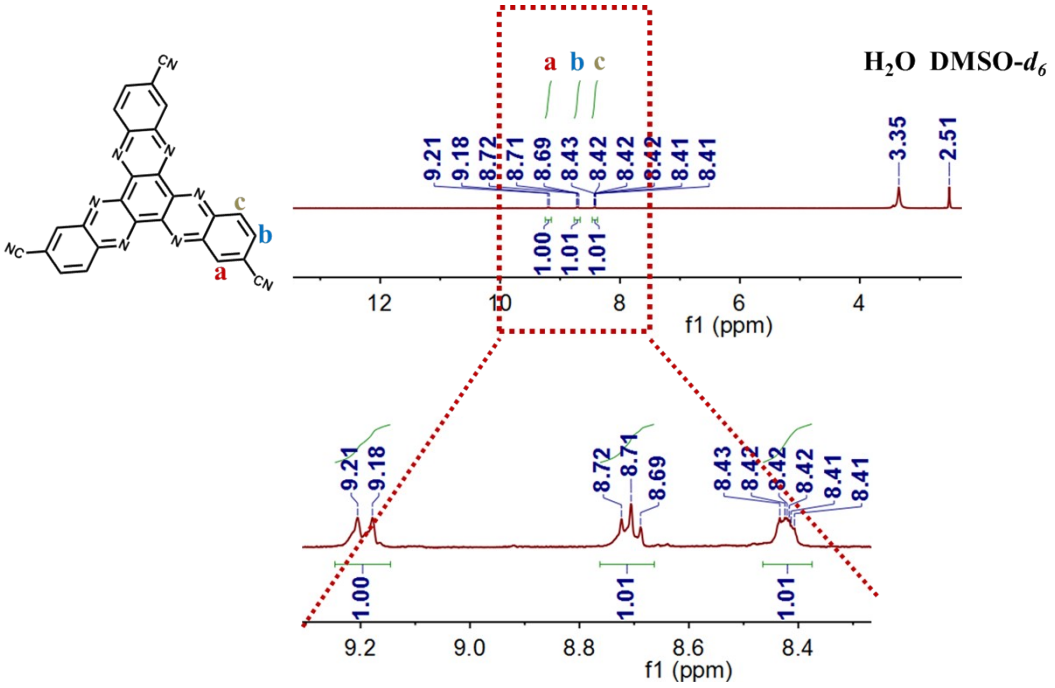

Figure S8. The ^{1}H NMR spectrum of HATN-3CN.

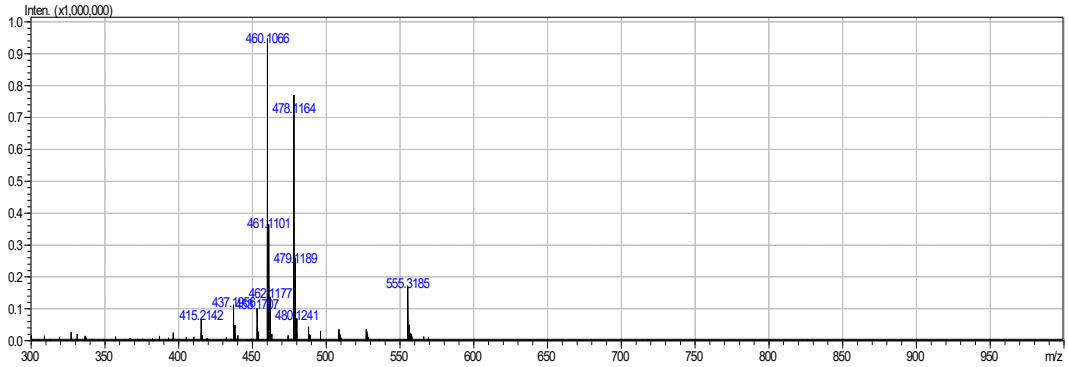

Figure S9. HR-MS mass spectroscopy of HATN-3CN.

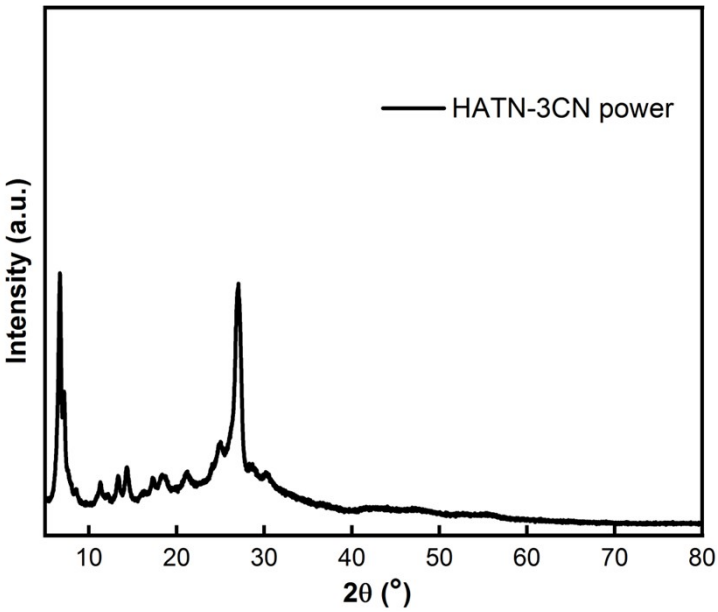

Figure S10. PXRD of HATN-3CN power.

(a)

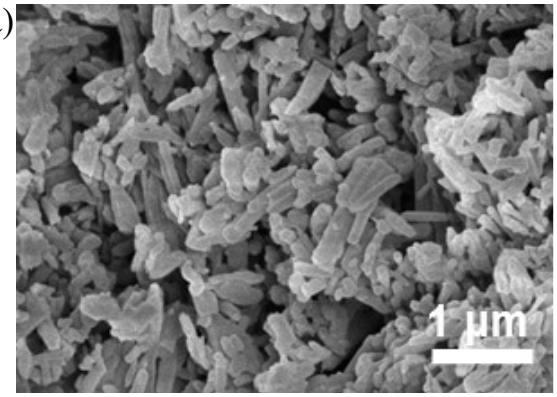

(b)

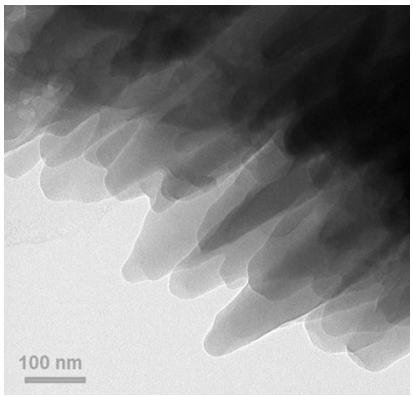

Figure S11. SEM images(a) and TEM images (b) of HATN-3CN power.

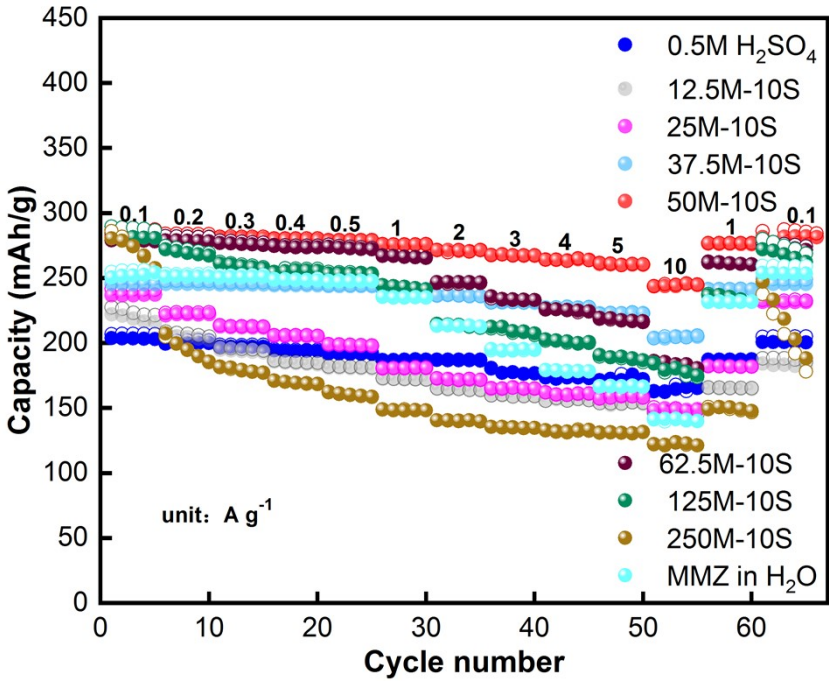

Figure S12. The rate performance of HATN-3CN under different ratios MMZ of electrolyte.

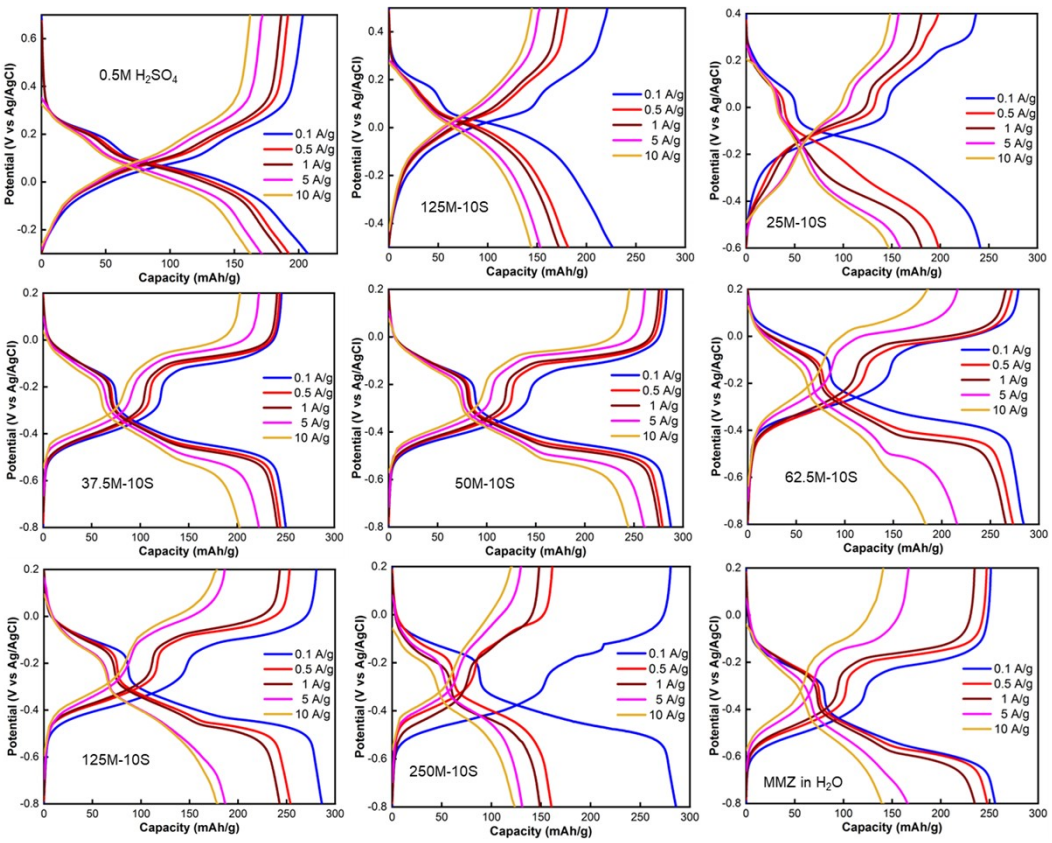

Figure S13. The charge-discharge curves of HATN-3CN electrode in a series of electrolytes.

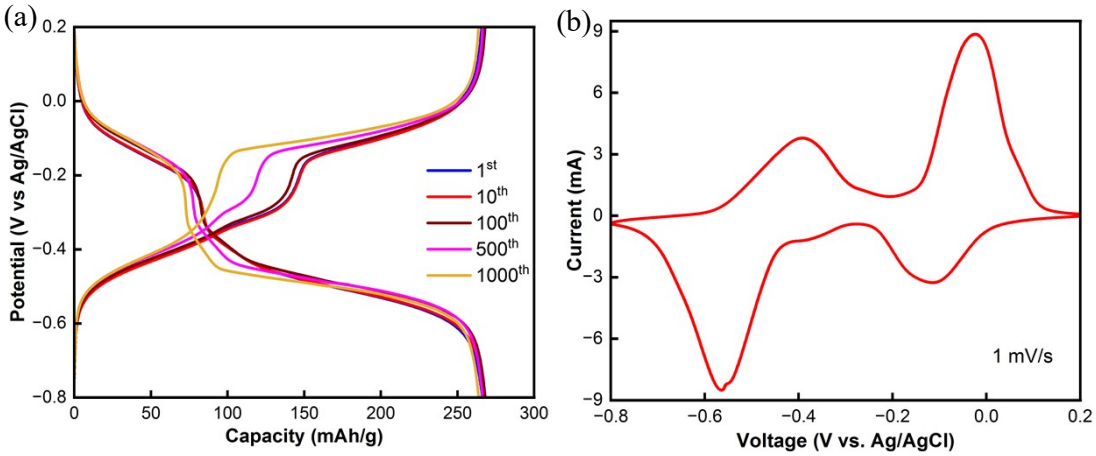

Figure S14. (a) The GCD curves of HATN-3CN of 1st, 10th, 100th, 500th and 1000th cycle and (b) CV curve of HATN-3CN after 1000 cycles in 50M-10S electrolyte.

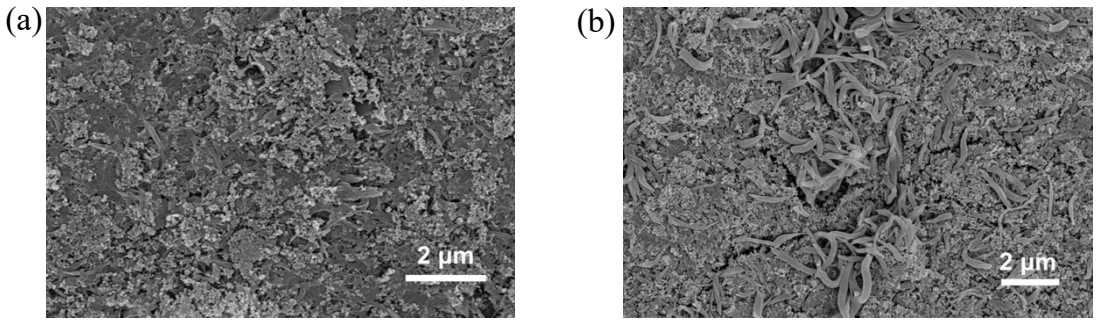

Figure S15. SEM images of HATN-3CN electrode in (a) initial state and (b) after 1000 cycles.

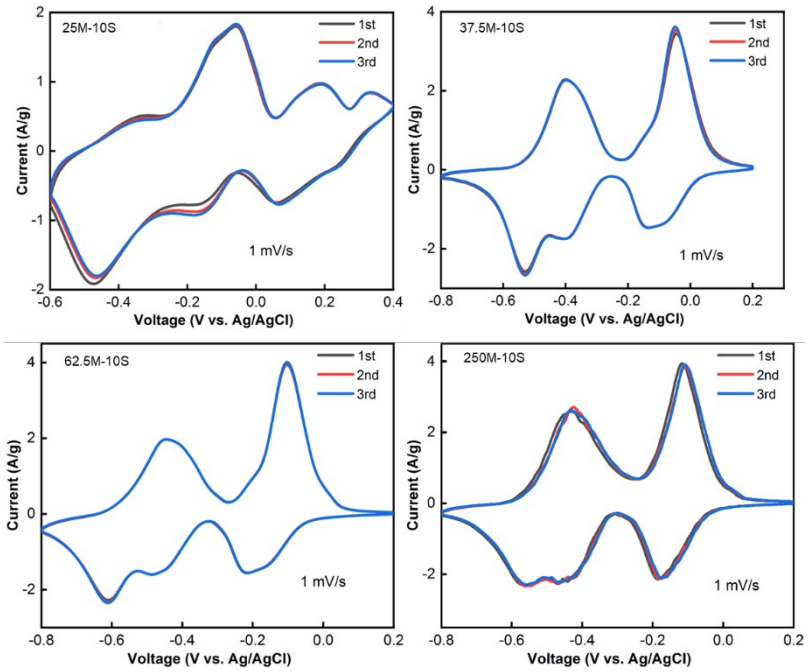

Figure S16. The CV curves of HATN-3CN electrode in different electrolytes.

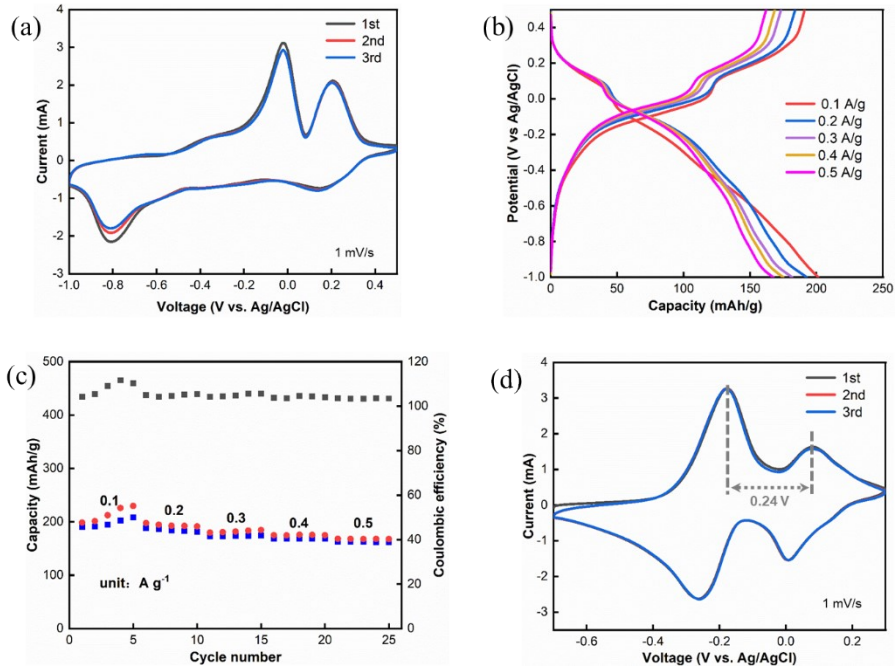

Figure S17. (a) The CV curve, (b) charge-discharge curve and (c) rate curve of HATN-3CN electrode in 1 M DMMZC electrolyte. (d) CV curves of HATN-3CN electrode in MTZ-H_2SO_4 electrolyte.

Note: MTZ-H_2SO_4 electrolyte was obtained by mixing 1 mL of MTZ with 1 mL of H_2O and 0.2 mL of 0.5 M H_2SO_4.

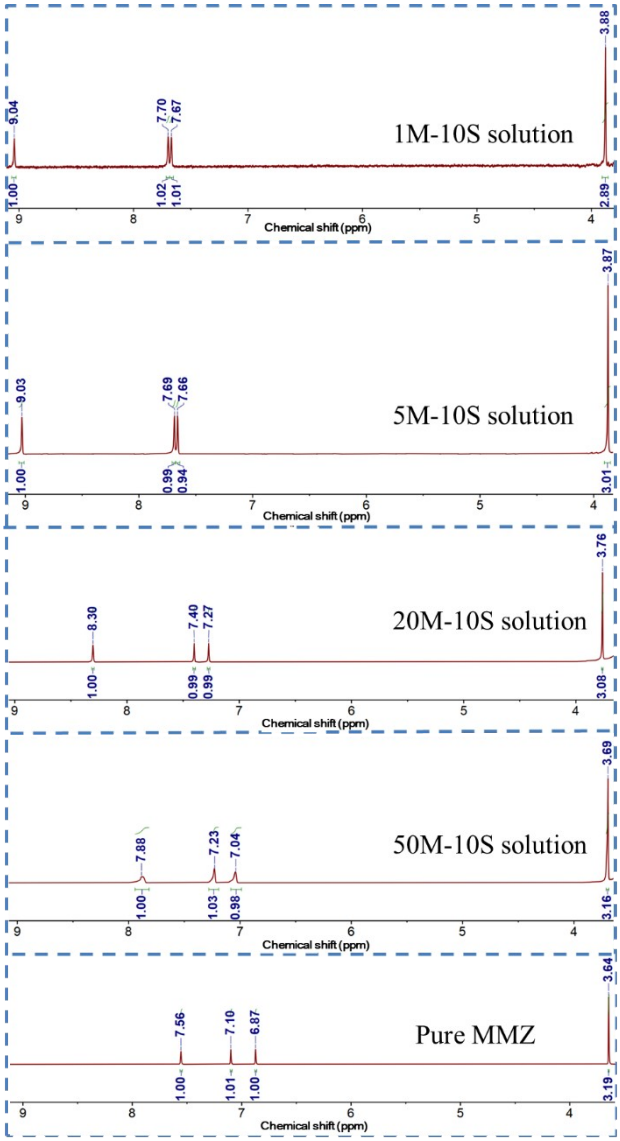

Figure S18. (a) ^{1}H-NMR spectra of different molar ratios of MMZ/H_2SO_4. The solvents used for the ^{1}H-NMR spectra were DMSO-d_6.

Note: MMZ/H_2SO_4 solutions were configured similarly to the M-S electrolyte. Taking the 1M-10S solution as an example, the solution was obtained by mixing 8 μL of MMZ with 2 mL of 0.5 M H_2SO_4, and the mol ratio of MMZ to $H_2SO_4$was 1:10. The chemical shifts of the imidazolium ion's four hydrogens (m, n, o, p likely the one labeled in figure 4f) are shown from left to right in the figure S18.

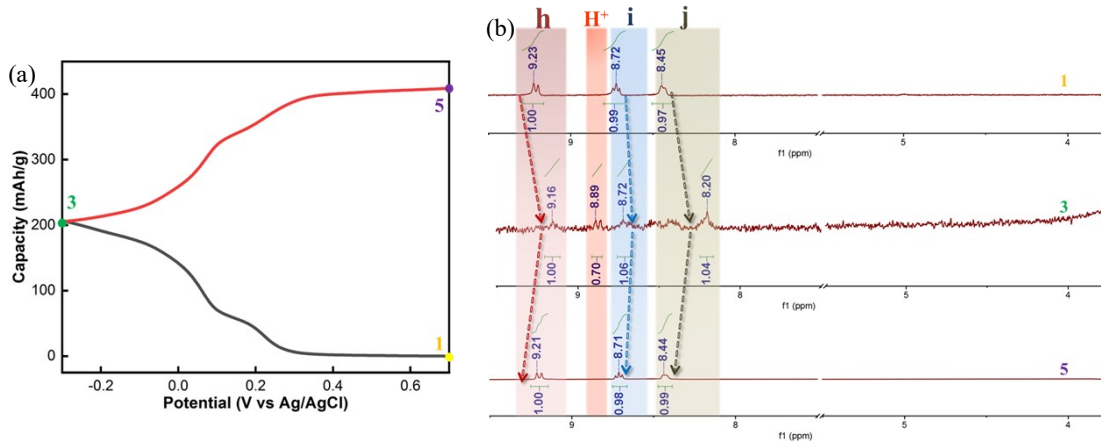

Figure S19. (a) Indication of different charge and discharge states, and (b) Ex situ ^{1}H-NMR spectra of HATN-3CN electrodes in 0.5 M H_2SO_4.

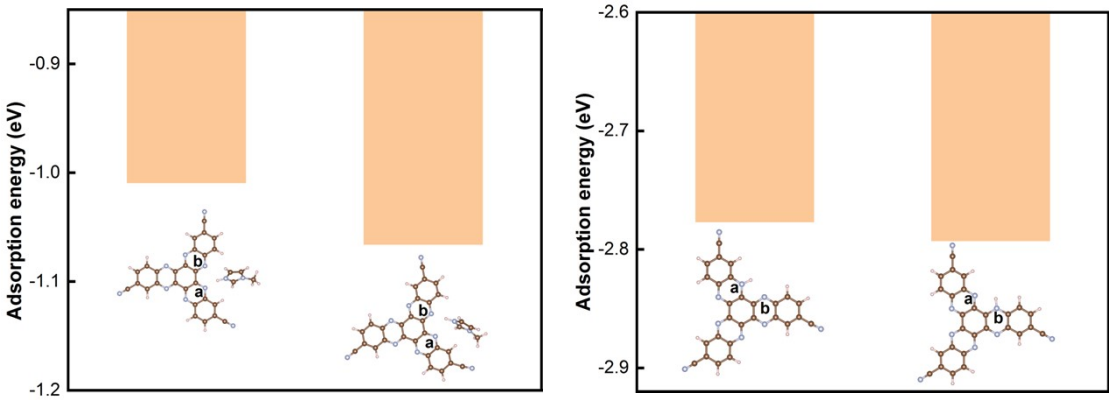

Figure S20. The adsorption energy calculations of different sites.

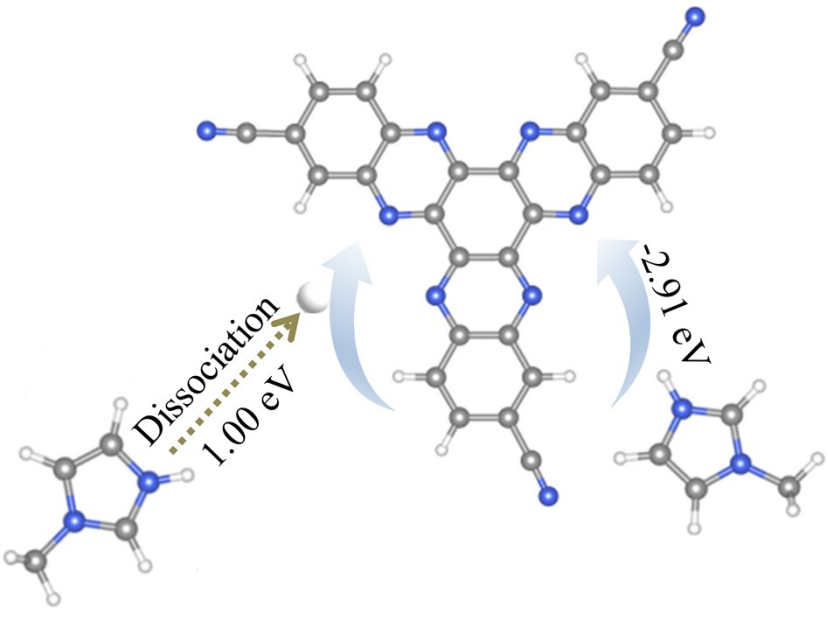

Figure S21. The energy calculation for different insertion methods.

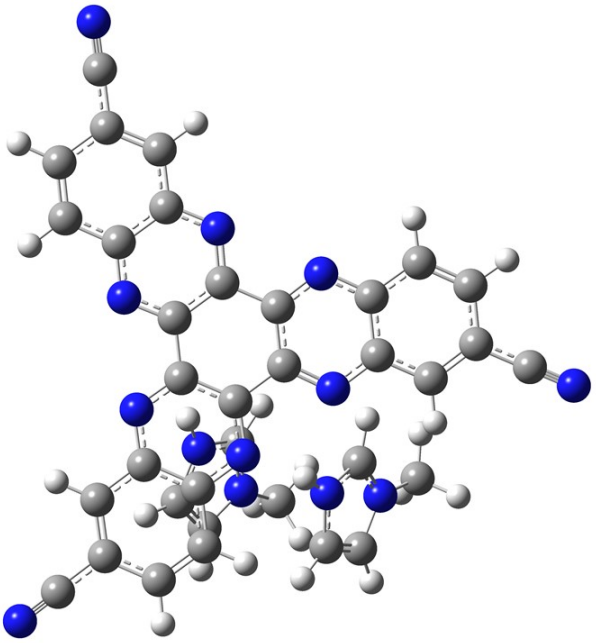

Figure S22. Structural optimization diagram of two MMZ-H^+ insertions.

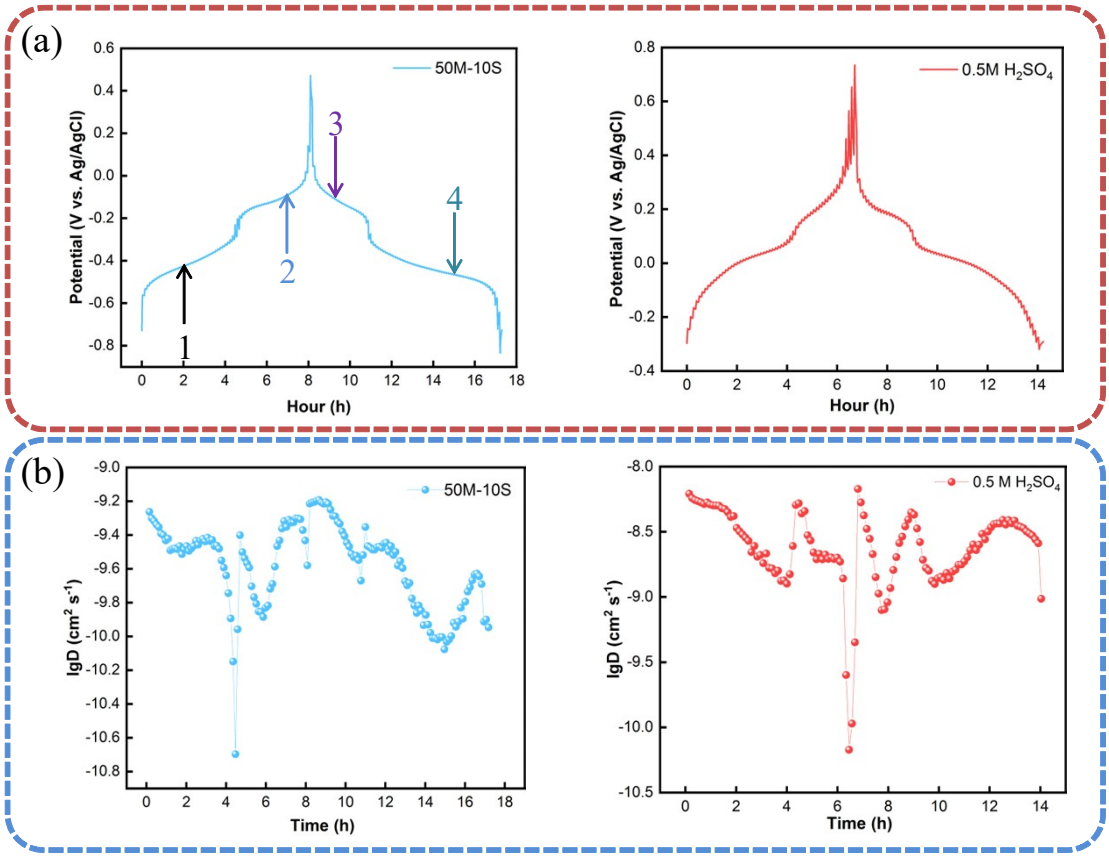

Figure S23. (a) GITT profiles of HATN-3CN electrode and (b) ion diffusion coefficients in 50M-10S electrolyte and 0.5 M H_2SO_4.

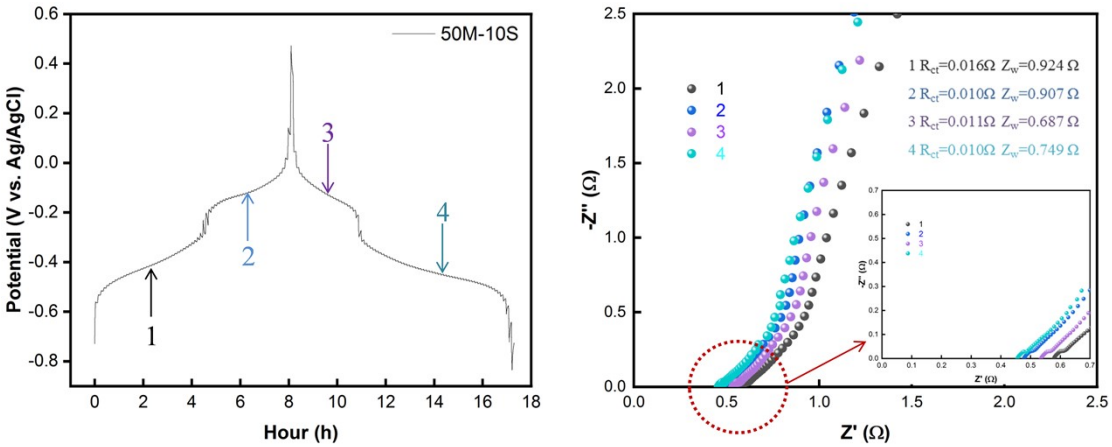

Figure S24. The EIS test of HATN-3CN electrode in 50M-10S electrolyte.

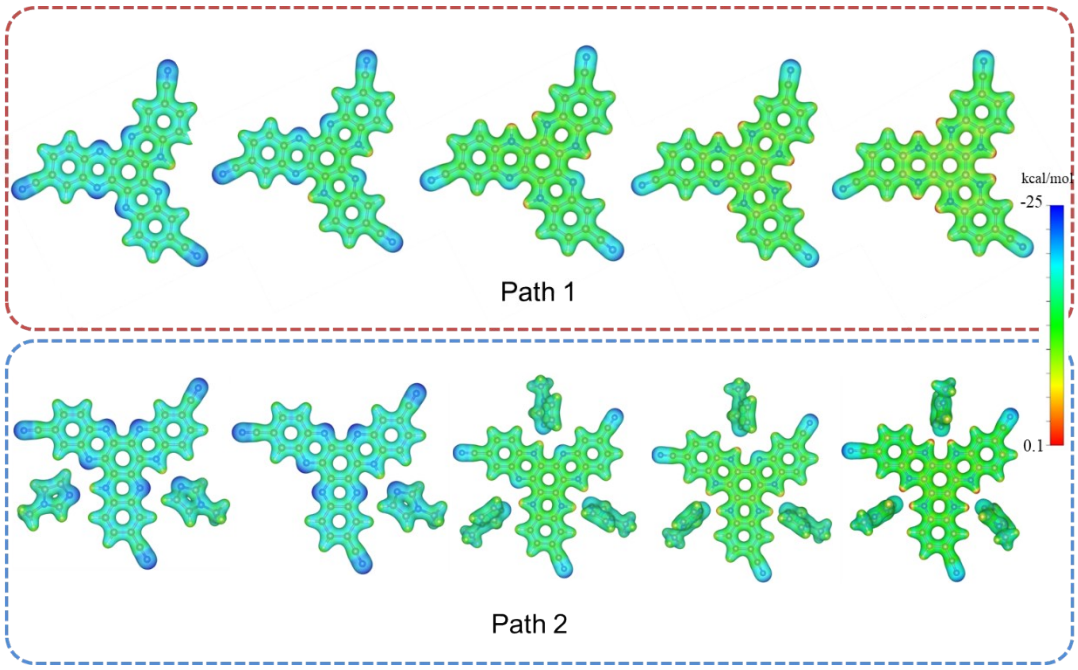

Figure S25. Calculation of MESP distribution of HATN-3CN.

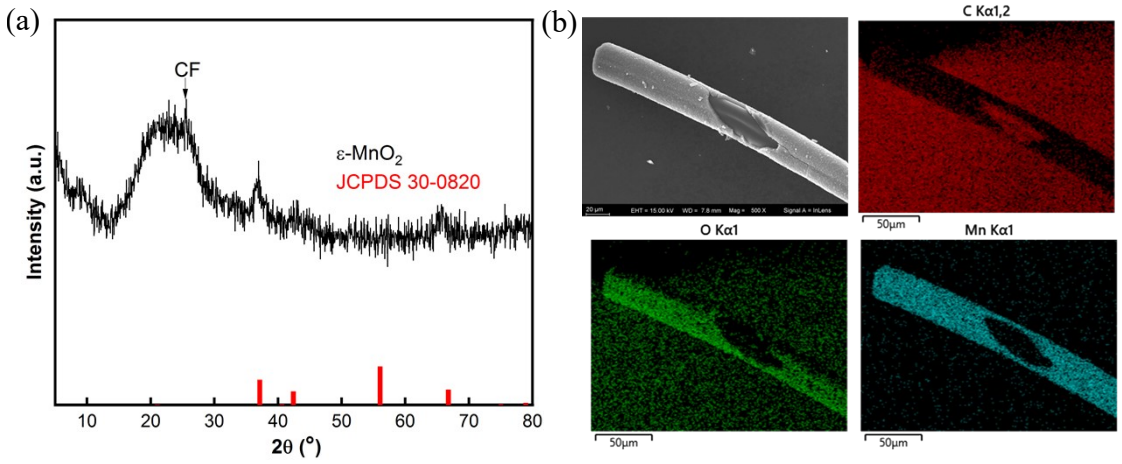

Figure S26. Physical characterizations of MnO_2. (a) XRD pattern. (b) SEM images and EDS elemental mapping images for MnO_2 in carbon fiber.

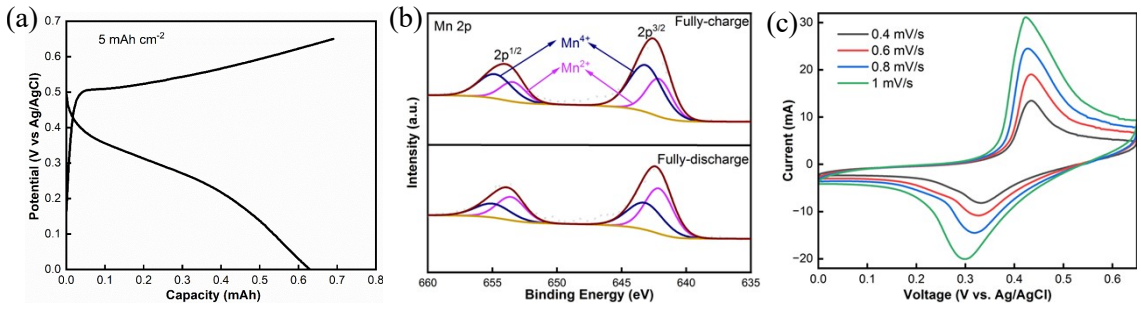

Figure S27. (a) The charge-discharge curves and (b) XPS change during the charging and discharge process and (c) CV curves of MnO_2 electrode.

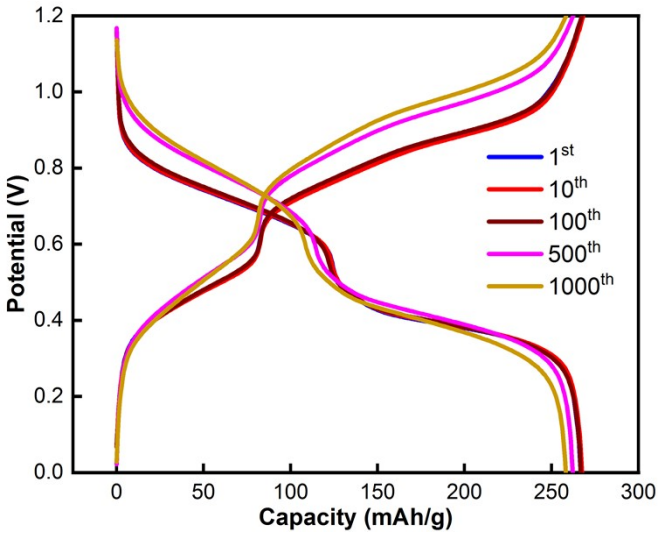

Figure S28. The GCD curves of HATN-3CN of 1st, 10th, 100th, 500th and 1000th cycle of full cell after 1000 cycles in 0.5 M $MnSO_4$ + 50M-10S electrolyte.

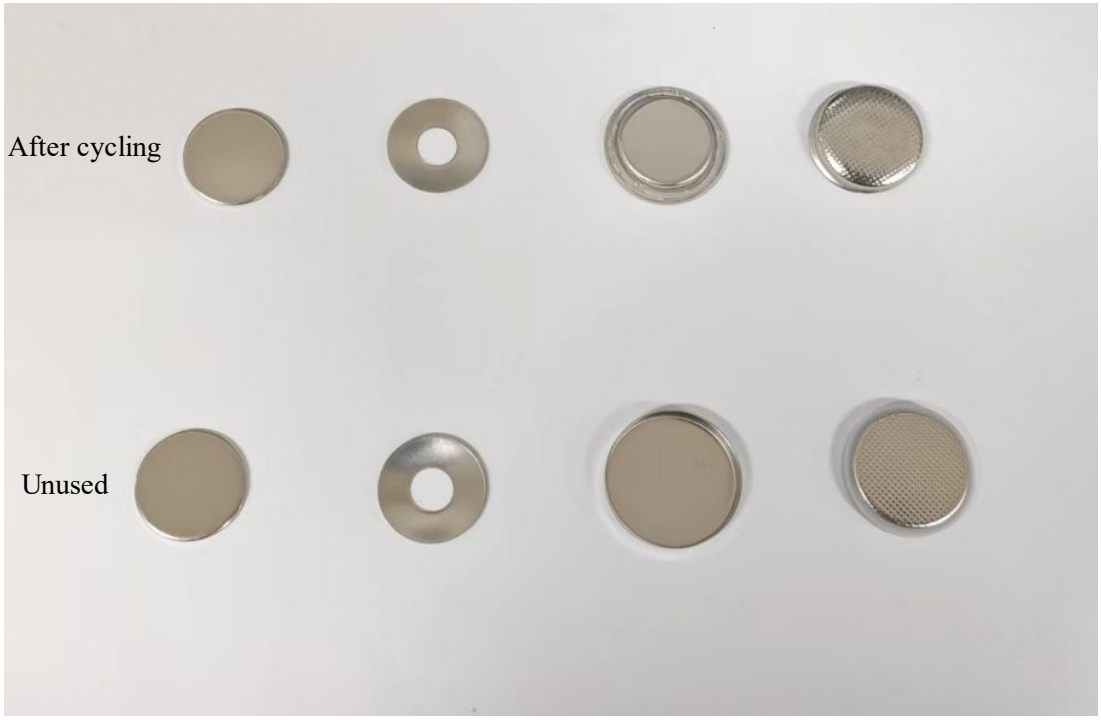

Figure S29. The digital image of battery cases after cycling in 0.5 M $MnSO_4$ +50M-10S electrolyte (top) and unused (bottom).

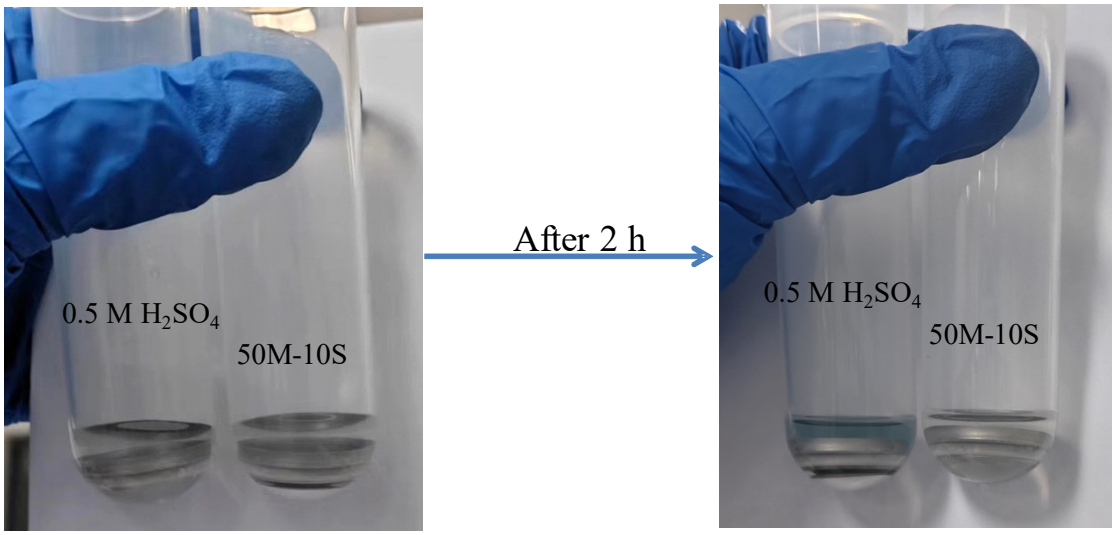

Figure S30. The digital image of components of 2032 coin cell soaked in different circumstances.

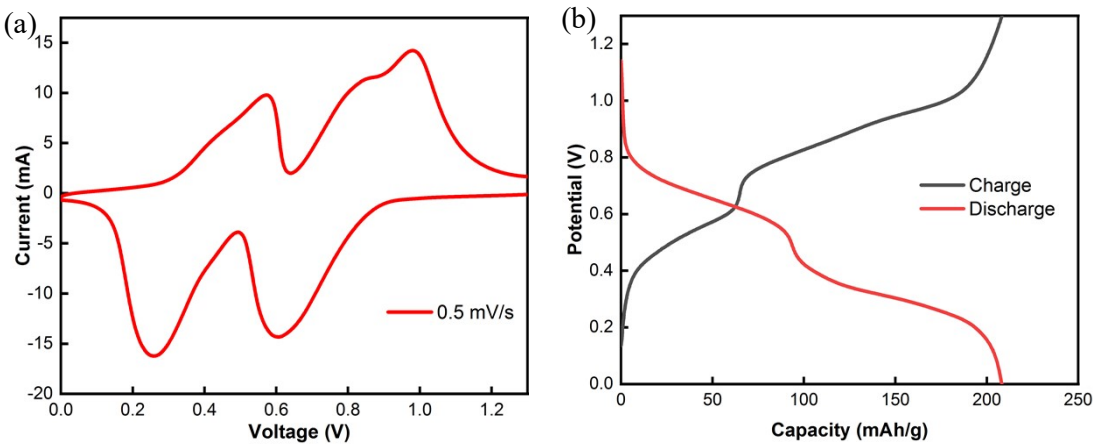

Figure S31. CV (a) and GCD curves (b) of HATN-3CN//MnO_2 pouch cell.

Note: The pouch cell was designed and fabricated with HATN-3CN, MnO_2, glass microfiber and 0.5M $MnSO_4$+50M-10S as anode, cathode, separator and electrolyte. Carbon cloth was working as current collector (3 x 3 cm) and tab at the same time. The loading mass of HATN-3CN is 16.2 mg.

Table S5. Comparison of recently reported proton battery electrolytes with full cell configuration.

Electrodes	Electrolytes	Ions type	Cycling stability (specific capacity/based on; current density; cycles; capacity retention)	Reference
HATN-3CN//MnO_2	0.5 M $MnSO_4$ in 50M-10S electrolyte	MMZ-H^+ & H^+	266.6mAh g^{-1}/anode, 1 A g^{-1} , 1000, 97 %	This work
PTO//MnO_2	2.0 M H_2SO_4 +2.0 M $MnSO_4$	H^+	203.4 mAh g^{-1}/-, 3 A g^{-1} , 400, 88 %	Ref.[13]
PTO//MnO_2@GF	2.0 M H_2SO_4 +2.0 M $MnSO_4$	H_3O^+	150 mAh g^{-1}/anode, 2.5 C , 5000, 80 %	Ref.[14]
MoO3@TiO_2//MnO_2	1.0 M H_2SO_4 +1.0 M $MnSO_4$	H^+	~200 mAh g^{-1}/anode, 10 A g^{-1}, 500, 80 %	Ref.[15]
ALO // MnO2@CF	2 M H_2BF_4 +2M $MnBF_4$	H^+	145 mAh g^{-1}/anode, 5 A g^{-1} , 300, 80 %	Ref.[16]
AC//VPO_4F	H_3PO_4 in MeCN	H^+	42 mAh g^{-1}/cathode, 0.2 A g^{-1}, 300, 72%	Ref.[17]
PTCDI//Ni-APW	1.0M $(NH_4)_2SO_4$	NH_4^+	35 mAh g^{-1}/total mass, 0.12 A g^{-1},1000, 67%	Ref.[7]
PTCDI//KVO	22 M KCF_3SO_3 WiSE	K^+	~70 mAh g^{-1}/cathode, 10 C, 20000, 77.3%	Ref.[18]
Zn//PTD-1	2 M $ZnSO_4$	H^+ & SO_4^{2-}	~125mAh g^{-1}/cathode, 1 A g^{-1}, 4000, 82.5%	Ref.[19]
Zn//6CN-HAT@MXene	2 M $Zn(CF_3SO_3)_2$	Zn^{2+} & H^+	200 mAh g^{-1}/cathode, 5 A g^{-1}, 5000, 90%	Ref.[20]

PAQS//$Ni(OH)_2$	10 M KOH	K^+ & H^+	180 mAh g^{-1}/-, 0.2 A g^{-1}, 1350, 88%	Ref.[21]
HPP-COF// CoNi-LDH	1 M NaOH	Na^+	119.6 mAh g^{-1}/ anode, 30 A g^{-1},10000, 70.6%	Ref.[22]

Reference

[1] G. W. T. M. J. Frisch, H.B. Schlegel, G.E. Scuseria, M.A. Robb, J.R. Cheeseman, G. Scalmani, V. Barone, G.A. Petersson, H. Nakatsuji, X. Li, M. Caricato, A.V. Marenich, J. Bloino, B.G. Janesko, R. Gomperts, B. Mennucci, D.J. Hratch. , Revision C.01 Gaussian, Inc., Wallingford CT Revision C.01 Gaussian, Inc., Wallingford CT (2016).

[2] F. U. S. Yong-Lei Wang, Sergei Glavatskih, Oleg Antzutkin, Aatto Laaksonen., Atomistic insight into orthoborate-based ionic liquids: Force field development and evaluation, J. Phys. Chem. B 118 (2014) 8711-8723.

[3] T. M. Mark James Abraham, Roland Schulz, Szilárd Páll, Jeremy C. Smith, Berk Hess, Erik Lindahl., High performance molecular simulations through multi-level parallelism from laptops to supercomputers., SoftwareX 1(2015).

[4] Kresse, G. & Furthmüller, J. Efficiency of ab-initio total energy calculations for metals and semiconductors using a plane-wave basis set. Comput. Mater. Sci. 6, 15–50 (1996).

[5] Perdew, J. P., Burke, K. & Ernzerhof, M. Generalized gradient approximation made simple. Phys. Rev. Lett. 77, 3865 (1996).

[6] Zhao, K. et al. Single-ion chelation strategy for synthesis of monodisperse Pd nanoparticles anchored in MOF-808 for highly efficient hydrogenation and cascade reactions. Nanoscale 14, 10980–10991 (2022).

[7] Momma, K.; Izumi, F. VESTA: A Three-Dimensional Visualization System for Electronic and Structural Analysis. *Journal of Applied crystallography* 2008, *41* (3), 653–658.

[8] Tirado-Rives, J.; Jorgensen, W. L. Performance of B3LYP Density Functional Methods for a Large Set of Organic Molecules. *Journal of chemical theory and computation* 2008, *4* (2), 297–306.

[9] Grimme, S.; Bannwarth, C.; Shushkov, P. A Robust and Accurate Tight-Binding Quantum Chemical Method for Structures, Vibrational Frequencies, and Noncovalent Interactions of Large Molecular Systems Parametrized for All Spd-Block Elements (Z = 1–86). *J. Chem. Theory Comput.* 2017, *13* (5), 1989–2009.

[10] Lu, T.; Chen, F. Multiwfn: A Multifunctional Wavefunction Analyzer. *Journal of computational chemistry* **2012**, *33* (5), 580–592.

[11] Wu X, Qi Y, Hong J J, et al. Rocking-Chair Ammonium-Ion Battery: A Highly Reversible Aqueous Energy Storage System[J]. Angewandte Chemie International Edition, 2017, 56(42): 13026-13030.

[12] Wang X, Yang Y, Lai C, et al. Dense-Stacking Porous Conjugated Polymer as Reactive-Type Host for High-Performance Lithium Sulfur Batteries[J]. Angewandte Chemie International Edition, 2021, 60(20): 11359-11369.

[13] Wu S, Guo H, Su Z, et al. Suppressed Manganese Oxides Shuttling in Acidic Electrolytes Extends Shelf-Life of Electrolytic Proton Batteries[J]. Advanced Functional Materials, 2024, 34(28): 2315706.

[14] Guo Z, Huang J, Dong X, et al. An organic/inorganic electrode-based hydronium-ion battery[J]. Nature Communications, 2020, 11(1): 959.

[15] Wang C, Zhao S, Song X, et al. Suppressed Dissolution and Enhanced Desolvation in Core–Shell MoO3@TiO2 Nanorods as a High-Rate and Long-Life Anode Material for Proton Batteries[J]. Advanced Energy Materials, 2022, 12(19): 2200157.

[16] Sun T, Du H, Zheng S, et al. High Power and Energy Density Aqueous Proton Battery Operated at −90 °C[J]. Advanced Functional Materials, 2021, 31(16): 2010127.

[17] Liao M, Cao Y, Li Z, et al. VPO4F Fluorophosphates Polyanion Cathodes for High-Voltage Proton Storage[J]. Angewandte Chemie International Edition, 2022, 61(32): e202206635.

[18] Liang G, Gan Z, Wang X, et al. Reconstructing Vanadium Oxide with Anisotropic Pathways for a Durable and Fast Aqueous K-Ion Battery[J]. ACS Nano, 2021, 15(11): 17717-17728.

[19] Wang N, Guo Z, Ni Z, et al. Molecular Tailoring of an n/p-type Phenothiazine Organic Scaffold for Zinc Batteries[J]. Angewandte Chemie International Edition, 2021, 60(38): 20826-20832.

[20] Zhao D, Li Z, Xu D, et al. Multiple Redox-Active Cyano-Substituted Organic Compound Integrated with MXene Nanosheets for High-Performance Flexible Aqueous Zn-Ion Battery[J]. Advanced Functional Materials, 2024, 34(25): 2316182.

[21] Liang Y, Jing Y, Gheytani S, et al. Universal quinone electrodes for long cycle life aqueous r echargeable batteries[J]. Nature Materials, 2017, 16(8): 841-848.

[22] Lin Y, Cui H, Liu C, et al. Inside Back Cover: A Covalent Organic Framework as a Long-life and High-Rate Anode Suitable for Both Aqueous Acidic and Alkaline Batteries [J].

Angewandte Chemie International Edition, 2023, 62(14): e202302702.